Materials Horizons

ROYAL SOCIETY OF CHEMISTRY

COMMUNICATION

View Article Online
View Journal

Cite this: DOI: 10.1039/d2mh00844k

Received 6th July 2022,
Accepted 13th September 2022

DOI: 10.1039/d2mh00844k

rsc.li/materials-horizons

Super-soft, firm, and strong elastomers toward replication of tissue viscoelastic response†

Erfan Dashtimoghadam, [a] Mitchell Maw, [a] Andrew N. Keith,[a] Foad Vashahi, [a] Verena Kempkes,[a] Yulia D. Gordievskaya, [b] Elena Yu. Kramarenko, [b] Egor A. Bersenev, [b] Evgeniia A. Nikitina, [b] Dimitri A. Ivanov, *[bcd] Yuan Tian, [a] Andrey V. Dobrynin, *[a] Mohammad Vatankhah-Varnosfaderani*[a] and Sergei S. Sheiko *[a]

Polymeric networks are commonly used for various biomedical applications, from reconstructive surgery to wearable electronics. Some materials may be soft, firm, strong, or damping however, implementing all four properties into a single material to replicate the mechanical properties of tissue has been inaccessible. Herein, we present the A-*g*-B brush-like graft copolymer platform as a framework for fabrication of materials with independently tunable softness and firmness, capable of reaching a strength of ~10 MPa on par with stress-supporting tissues such as blood vessel, muscle, and skin. These properties are maintained by architectural control, therefore diverse mechanical phenotypes are attainable for a variety of different chemistries. Utilizing this attribute, we demonstrate the capability of the A-*g*-B platform to enhance specific characteristics such as tackiness, damping, and moldability.

New concepts

Soft tissues are protected from accidental trauma by two intrinsic defense mechanisms: strain-adaptive stiffening and shock absorbance. Although many synthetic materials can replicate tissue softness, matching tissue strength and viscoelastic response remains challenging. We report the A-*g*-B brush-like graft copolymer platform for the design of thermoplastic elastomers as a framework for full replication of tissue softness, firmness, strength, and energy dissipation. While the bottlebrush B-block facilitates material softness, microphase separation of randomly grafted A-blocks yields a reversible physical network that concurrently enhances mechanical resilience and damping. Unlike the conventional "one molecule – one strand" approach to the network construction, one A-*g*-B molecule spans multiple meshes, which reinforces the integrity of the stress-supporting scaffold. Furthermore, the design-by-architecture approach empowers architectural programming of mechanical properties at a given chemical composition by adjusting dimensions of the A and B blocks. Reciprocally, the platform allows tuning of the A-*g*-B chemistry at a given architecture for a desired mechanical profile to satisfy application specific needs, such as moldability, tackiness, and controlled swellability. The synergistic combination of the architectural and chemical control enables precise and predictable property regulation of elastomeric materials for a broad range of practical applications including but not limited to biomedical devices, pressure-sensitive adhesives, and additive manufacturing.

Introduction

Combining softness, firmness, strength, and damping into a neat material is incompatible with current polymer network designs, yet such a combination is commonplace in biological tissues.[1–11] Initially very soft tissues (Young's modulus: $E_0 \sim 10^2$–10^5 Pa) stiffen rapidly with deformation, empowering up to a 1000-fold modulus increase (aka firmness) and the ability to withstand >10 MPa stress-at-break for protection of delicate organs against accidental rupture. Additional protection is provided by a relatively high damping factor ($\tan\delta$) ranging from 0.1 of skin to 0.7 of brain tissue, which allows for absorbing shocks and vibrations in a broad frequency range. This combination of distinct mechanical traits is enabled by a hierarchical scaffold of collagen fibers that endorse a cascade of molecular deformation mechanisms activated at different stress levels.[12] Implementation of such self-organization principles in synthetic materials is challenging.

Despite recent advances in replicating tissue's softness and strain-stiffening,[13–19] integrating softness with tissue-comparable strength remains elusive. Successful efforts to increase the strength and toughness of elastomers through double networks typically lead to a considerable modulus increase ($E_0 > 10^6$ Pa).[20–22] On the other hand, advancements in the design of super-soft elastic materials suffer from consequentially low strength.[23,24]

[a] Department of Chemistry, University of North Carolina at Chapel Hill, 27599, USA. E-mail: sergei@email.unc.edu, mvatan@live.unc.edu, avd@email.unc.edu
[b] Lomonosov Moscow State University, Leninskie Gory 1, 119991, Moscow, Russian Federation
[c] Institut de Sciences des Matériaux de Mulhouse-IS2M, CNRS UMR 7361, 15, rue Jean Starcky, F-68057 Mulhouse, France. E-mail: dimitri.ivanov@uha.fr
[d] Sirius University of Science and Technology, 1 Olympic Ave, 354340, Sochi, Russian Federation

† Electronic supplementary information (ESI) available. See DOI: https://doi.org/10.1039/d2mh00844k

Herein, we present the bottlebrush graft copolymer (A-*g*-B) platform, which delivers robust physical networks where a single molecule connects multiple meshes (as designated by the bold backbone) empowering a unique combination of softness, firmness, and strength (Fig. 1a). Furthermore, this platform accommodates broad chemical diversity of the A and B blocks to satisfy needs of specific applications such as tissue-mimetic elastomers for biomedical devices, soft robotics, wearable electronics, pressure-sensitive adhesives, and additive manufacturing.

Incorporation of bottlebrush macromolecules into elastomers has led to a breakthrough in mechanical property control of polymer networks.[25,26] Due to the architectural disentanglement of brush-like strands,[27–31] it became possible to prepare super-soft elastomers with a modulus down to 100 Pa (Fig. 1b).[32,33] However, brush networks with covalent crosslinks show relatively low firmness, $\beta < 0.2$, defined by the strain-stiffening parameter $\beta = \langle R_{in}^2 \rangle / R_{max}^2$ – a ratio of the mean square end-to-end distance, $\langle R_{in}^2 \rangle$, of undeformed strands to their contour length, R_{max}.[14,34,35] Firmness was subsequently increased through the design of ABA block copolymer networks (middle panel, Fig. 1a), where the bottlebrush backbones get additionally extended by microphase segregation of A and B

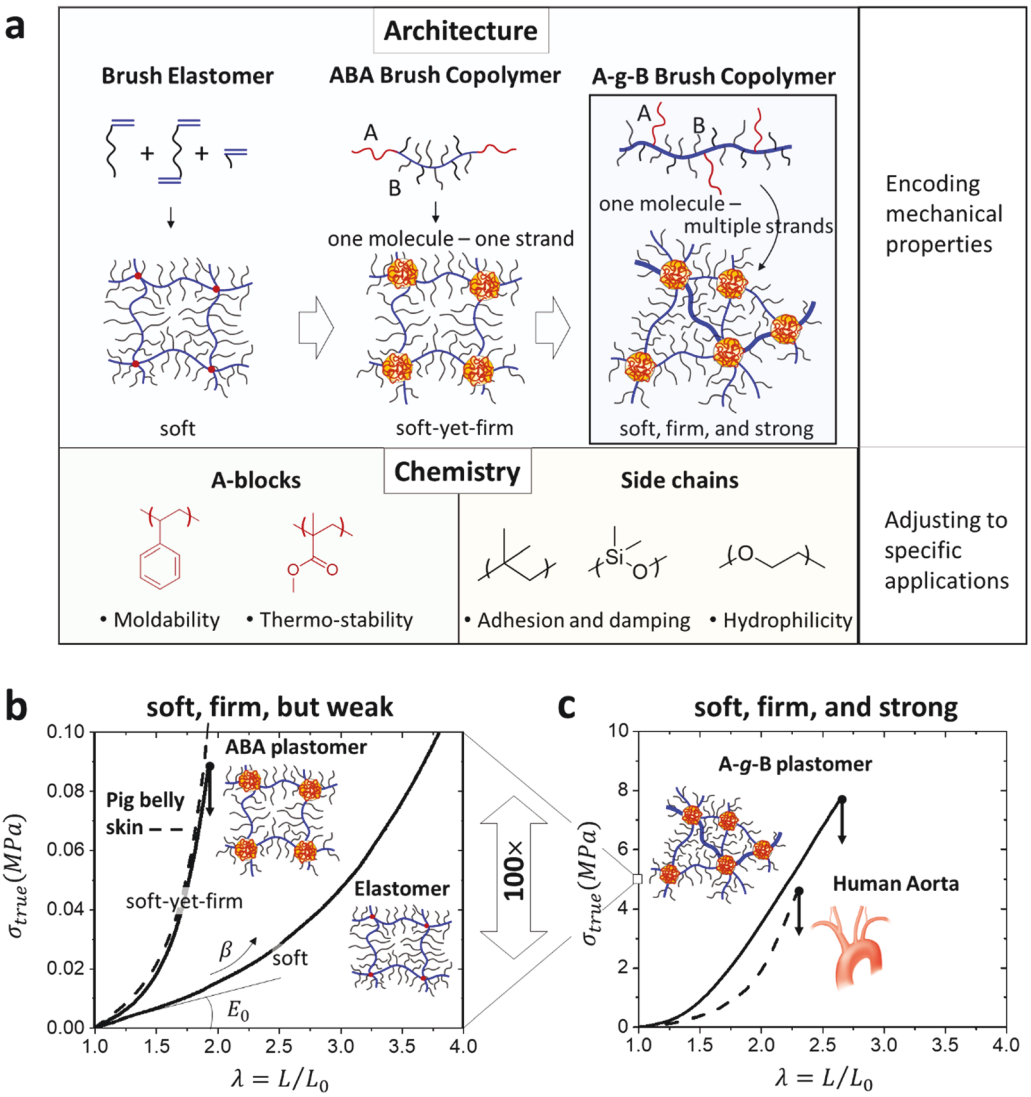

Fig. 1 (a) Evolutionary augmentation of mechanical properties from super-softness of covalent bottlebrush elastomers through adding firmness in self-assembled ABA networks to superior strength of molecularly interconnected A-*g*-B elastomers. The mesh interconnectivity is highlighted by a bold backbone of an A-*g*-B macromolecule. Interplay of multiple architectural parameters, such as length and grafting density of side chains in the B block as well as A block dimensions, permits unparalleled control of equilibrium and viscoelastic mechanical properties. Chemistries chosen for application specific functions, such as adhesion, moldability, or water uptake, can be implemented within specific mechanical phenotypes. (b) Stress–elongation curves of selected covalent bottlebrush elastomer (E_0 = 9.9 kPa and β = 0.07) and a thermoplastic ABA brush copolymer (E_0 = 13.3 kPa and β = 0.77) samples. Although, the ABA system demonstrates very high firmness that may reach $\beta \cong 0.9$ on par with skin (dashed line), both systems exhibit low strength ($\sigma_{max} < 0.1$ MPa).[15] (c) Self-assembled networks of A-*g*-B brush-like graft copolymers display a unique combination of softness, firmness, and strength (ESI,† Table S1). A sample of PBA-*ran*-PMMA-*g*-(PDMS/PS) graft copolymer exhibits strength ~8 MPa on par with aorta (dashed line), surpassing many other strong tissues.

blocks yet remain stretchable due to the "hidden length" of coiled A-blocks inside the network nodes.[13,36] These thermoplastic elastomers with bottlebrush strands demonstrated unprecedented firmness up to $\beta \cong 0.9$ on par with biological tissues, while maintaining the tissue-like softness ($E_0 \cong 10^3$–10^5 Pa) and extensibility ($\lambda_{max} \cong 2$–4) (Fig. 1b). However, the ABA systems possess a relatively low strength of $\sigma_{max} < 0.5$ MPa, which is ~10 times weaker than that of stress-supporting tissues such as skin and blood vessels (ESI,† Table S1).[13,15] The low strength is ascribed to the "one strand – one molecule" construction, where the deformation-caused withdrawal of an A block from a network node leads to its coiling and strand removal from the load-bearing scaffold.[13,36] To address this issue, we introduce A-*g*-B bottlebrush graft copolymers ("-*g*-" denotes long A-blocks randomly grafted to a bottlebrush backbone of block B), where one brush molecule may span multiple network cells to enhance network resilience (Fig. 1c). When an A-block is dislodged from an A-domain during deformation, the corresponding strand remains strained, which concurrently maintains the load-bearing scaffold, improves tension distribution, and allows for re-association of the loose A-block with neighboring A-domains. Even though the A-*g*-B networks are less perfectly organized than the ABA networks, they demonstrate ~10–100 × strength enhancement compared to ABA systems, attaining σ_{max} = 8 MPa greater than human aorta (Fig. 1c and ESI,† Table S1).[37] Furthermore, self-assembled A-*g*-B networks can be reversibly disassembled either by heating above the order–disorder temperature or dissolution in a good solvent, which enhances materials processability.

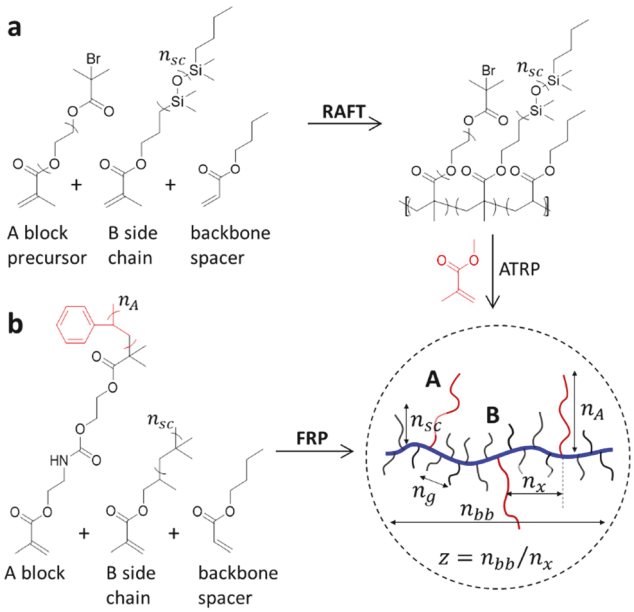

Fig. 2 Polymerization of A-*g*-B brush-like graft copolymers with controlled grafting density of the brush (B) block and fraction of linear A blocks distributed as long side chains in the brush block. (a) The controlled radical polymerization (CRP) of assorted macromonomers yields poly[*n*BA-*ran*-MMA-*g*-(PDMS/PMMA)] brush copolymers, while (b) the free radical polymerization (FRP) produces poly[*n*BA-*ran*-MMA-*g*-(PIB/PS)] brush copolymers with controlled DP of the brush block. The parameter n_x is defined as a ratio of molar ratio of A and B macromonomers, including spacers.

Results and discussion

Synthesis

A-*g*-B brush-like graft copolymers are defined by a set of six architectural parameters [n_{sc}, n_g, n_A, ϕ_A, n_{bb}, n_x], where n_{sc} is the degree of polymerization (DP) of the side-chains in the brush B block, n_g is the DP of backbone spacer between side chains, n_A and ϕ_A are respectively the DP and volume fraction of linear A-blocks, n_{bb} is the DP of a brush backbone, and n_x corresponds to the backbone DP between A-blocks equivalent to the DP of network strand (Fig. 2). For convenience of discussion, we also introduce parameter $z = n_{bb}/n_x$, which approximately corresponds to an average number of A-blocks per bottlebrush macromolecule. To study the effect of mesh interconnectivity on elastomer strength, we synthesized a series of A-*g*-B graft copolymers (similar to "Janus graft block copolymers")[38] with different z = 2–13 using a combination of reversible addition-fragmentation chain transfer (RAFT) co-polymerization of polydimethylsiloxane (PDMS) and Br-terminated poly(ethylene glycol) (PEG) macromonomers with consecutive atom transfer radical polymerization (ATRP) of poly(methyl methacrylate) (PMMA) A-block grafted from the terminal bromine, yielding poly[MMA-*g*-(PDMS/PMMA)] bottlebrush graft copolymers with n_g = 1 (Fig. 2 and ESI,† Table S2, Sections S1.2–S1.4).[39–45] To vary side chain grafting density (~n_g^{-1}), PDMS macromonomers were co-polymerized with *n*-butyl acrylate (BA) as backbone spacers between PDMS side chains yielding poly[*n*BA-*ran*-MMA-*g*-(PDMS/PMMA)] graft copolymers with n_g = 4–8 (Fig. 2a). For convenience, bottlebrush (densely grafted) samples will be referred to as PMMA-*g*-PDMS (n_g = 1), while the loosely grafted structures are named as PMMA-*g*-PDMS (n_g = 4, 8). Due to the difference in size and chemistry, moderate gradient of side chain and spacer distribution is assumed, though well-defined mechanical properties suggest minimal effect (Fig. S7, ESI†).[14] All synthesized samples are summarized in the (ESI,† Table S2), while representative A-*g*-B networks are in Table 1.

To demonstrate the universality of the platform and its modular nature in addressing specific applications, we prepared A-*g*-B graft copolymers with different chemical compositions of A-blocks and B-side chains. For example, PMMA A-blocks were replaced with polystyrene (PS) (ESI,† Sections S1.7, S1.8 and Scheme S3) to enable elastomer fluidity at ~100 °C for molding and 3D printing. By substituting PDMS side chains in the B-block with higher glass transition polyisobutylene (PIB) (ESI,† Section S1.6 and Scheme S2), we augmented viscoelastic dissipation at room temperature and conventional strain rates, thereby enhancing adhesion and vibration damping. For scalability, the controlled radical polymerization (CRP) methods were replaced with free radical polymerization (FRP) to synthesize PS-*g*-PDMS (n_g = 8) and PS-*g*-PIB (n_g = 8) (Fig. 2b).

Structure

Chemically dissimilar blocks undergo microphase separation.[46–49] Different techniques were employed for characterization of both

Table 1 Chemical structure and network morphology of brush-like graft copolymers

n_A [a]	ϕ_A [b]	n_g [c]	n_x [d]	n_{bb} [e]	E_0, [f] kPa	β [g]	d_1, nm	d_2, nm	d_3, nm	Q [h]	S_{in}, [i] nm^2	S_0, [j] nm^2
n_{bb} effect: poly[MMA-*g*-(PDMS/PMMA)]												
53	0.029	1	149	210	16.9	0.42	3.4	11.6	28.5	107	2.0	9.9
63	0.034	1	149	607	26.6	0.45	3.4	14.5	31.1	175	1.9	9.9
62	0.034	1	149	1935	31.4	0.40	3.4	14.9	32.0	193	1.8	9.9
n_A effect: poly[MMA-*g*-(PDMS/PMMA)]												
27	0.015	1	149	1935	9.8	0.31	3.4	13.3	36.1	316	0.9	9.9
62	0.034	1	149	1935	31.4	0.40	3.4	14.9	32.0	193	1.8	9.9
81	0.044	1	149	1935	53.1	0.46	3.4	13.6	27.6	125	2.5	9.9
n_g effect: poly[*n*BA-*ran*-MMA-*g*-(PDMS/PMMA)]												
81	0.044	1	149	1935	53.1	0.46	3.4	13.6	27.6	125	2.5	10.0
178	0.241	4	139	1923	103	0.29	3.5	16.9	29.1	98	4.6	10.6
147	0.278	8	142	1959	60.9	0.13	3.9	16.7	31.2	115	3.8	13.2
n_x effect: poly[*n*BA-*ran*-MMA-*g*-(PDMS/PS)]												
60	0.05	8	502	1061	78	0.18	3.7	12.7	20.3	106	2.4	11.7
60	0.08	8	315	2807	110	0.22	3.8	14.3	20.1	151	2.1	12.8
60	0.15	8	155	2854	528	0.44	4.0	16.1	18.9	215	1.9	13.9
60	0.24	8	86	4425	1853	0.72	3.6	15.6	18.4	196	2.0	10.9

[a] Number average DP of PS or PMMA side chains as determined by ^{1}H-NMR. [b] Volume fraction of PS or PMMA, ρ_{PS} = 1.02 g mL^{-1}, ρ_{PMMA} = 1.15 g mL^{-1}, ρ_{PDMS} = 0.96 g mL^{-1}. [c] Number of spacer repeat units between A blocks. [d] Number average DP of brush backbone between PS or PMMA side chains. [e] DP of total brush backbone in the A-*g*-B macromolecule. [f] Young's modulus determined either as tangent of a stress–strain curve at $\lambda \rightarrow 1$ or from the fitting eqn (S2) (ESI) at $\lambda = 1$ as $E_0 = E(1 + 2(1 - \beta)^{-2})/3$. [g] Strain-stiffening parameter $\beta = \langle R_{in}^2 \rangle / R_{max}^2$ obtained by fitting stress–strain curves with eqn (S1) (ESI). [h] Aggregation number. [i] Area per brush strand at the A/B interface calculated from the aggregation number as $S_{in} = \pi d_2^2/(2Q)$. [j] Apparent cross section area of bottlebrush cylinder $S_0 = \sqrt{3}/2 d_1^2$ assuming hexagonal packing.

molecular structure and morphology of self-assembled A-*g*-B networks. The copolymer composition [n_{sc}, n_g, n_A, n_x] was monitored by ^{1}H-NMR spectroscopy while samples with identical compositions but different n_{bb} were verified by the number average molecular weight from gel-permeation chromatography (ESI,† Fig. S5–S13). Atomic force microscopy (AFM) was used for molecular imaging of A-*g*-B macromolecules to confirm their dimensions and microphase separation (ESI,† Section S2.1). Langmuir–Blodget monolayers demonstrate densely packed worm-like PMMA-*g*-PDMS (n_g = 1) macromolecules (Fig. 3a and ESI,† Fig. S23), where the intermolecular distance of 8.3 ± 1.0 nm is consistent with two-fold the side chain contour length, $2R_{sc,max} = 2n_{sc}l \cong$ 8.7 nm, using n_{sc} = 14 and l = 0.31 nm as a projection length of the PDMS repeat unit. The dense monolayer arrangement hinders the microphase separation of the A-blocks, yet star-like aggregates of multiple bottlebrushes are evident in loosely packed films (Fig. 3b).

More insight into bulk morphology of A-*g*-B networks was obtained by small angle X-ray scattering (SAXS) (ESI,† Section S2.2). First, A-*g*-B samples of near identical [n_{sc},n_g,n_A, n_x] yet different n_{bb}, *i.e.* different numbers of A-blocks per backbone (z), are shown to produce nearly identical SAXS curves (Fig. 3d), which supports the hypothesis that long A-*g*-B macromolecules with $z > 2$ form topologically similar networks, differing only in mesh interconnectivity. Second, we show that the network morphology depends on the A-*g*-B architecture. Specifically, we studied (i) n_x variation at a given n_A (Fig. 3e), (ii) n_A variation at a given n_x (ESI,† Fig. S21), and (iii) variation of grafting density of B side chains (Table 1 and ESI,† Fig. S22). SAXS curves elicit three characteristic network dimensions: the interbrush distance (d_1), A-domain diameter (d_2), and the interdomain distance (d_3) (Fig. 3c and d). For densely grafted bottlebrush blocks (n_g = 1), d_1 corresponds to the brush diameter and the Kuhn length of the bottlebrush backbone ($b_K \cong d_1$).[35,50,51] From the domain diameter d_2 extracted from a series of ripples of the form-factor, we obtain two structural parameters: (i) aggregation number $Q = \rho V/M_A$ and (ii) interfacial area per brush strand $S_{in} = \pi d_2^2/(2Q)$, where ρ is mass density of A polymer, $V = \pi d_2^3/6$ – domain volume, and M_A – molecular mass of A-block (Table 1). Unlike the previously studied ABA linear-brush-linear copolymers,[13,15,52,53] each A block in an A-*g*-B macromolecule anchors two bottlebrush strands to a network node (Fig. 3c), which is accounted by the factor of 2 in the denominator of the S_{in} equation. As a result, the footprint of bottlebrush strands at the domain surface, S_{in}, is considerably smaller than the bottlebrush packing area in the bulk as $S_0 \cong \sqrt{3}/2 d_1^2$. This suggests strong extension of bottlebrush backbone at the interface, causing additional enhancement of the strain-stiffening response of A-*g*-B elastomers as discussed below.

Mechanical properties

Systematic studies of backbone dilution on the mechanical properties of brush networks by increasing n_{sc}, n_g^{-1}, and n_x have been established previously,[13,14] therefore, our main focus here is twofold: (i) strengthening the network through enhancement of mesh interconnectivity by increasing the number of A-blocks per brush macromolecules (z) and (ii) architecturally tuning the viscoelastic response. We conducted uniaxial tensile tests (ESI,† Section S2.3 and Fig. S25) of A-*g*-B brush networks with n_{bb} varying from ~200 to 2000 and z ranging from ~1.4 to 13 accordingly, while keeping the other architectural parameters (n_{sc}, n_g, n_x, n_A, ϕ_A) constant. All samples demonstrate similar softness, $E_0 \approx$ 50 kPa, and firmness, $\beta \approx$ 0.46–0.54 yet the σ_{max} increases 15-fold from 0.04 MPa to 0.9 MPa (Fig. 4a). This trend is corroborated by coarse-grained molecular dynamics simulations due to a direct increase in energy cost for A-block withdrawal in samples with a higher z-parameter (ESI,† Fig. S33 and S34). Although the achieved strengthening is substantial, the absolute values of $\sigma_{max} < 1$ MPa are relatively low. Additional strengthening was facilitated by concurrently decreasing grafting density of the side chains, n_g^{-1}, and increasing volume fraction of A blocks, ϕ_A (Fig. 4c). The decrease of grafting density reinforces the network by increasing volume fraction of the backbones. However, decreasing n_g^{-1} alone leads to a firmness decline as observed in covalent brush networks.[14,35] To reverse the trend, A-*g*-B's with greater volume fraction of A-blocks, ϕ_A, were synthesized. These elastomers witness a dual effect on network structure: (i) higher aggregation number of network nodes (Q), hence higher crosslink functionality and (ii) stronger strand extension, hence higher firmness (β) evidenced by the decreasing strand footprint (S_{in}) (Table 1). The series of PS-*g*-PDMS (n_g = 8) brush-like copolymers with ϕ_A ranging from 0.03 to 0.24 demonstrated steady increase of stress-at-break up to 6 MPa (Fig. 4c) which is comparable and even exceeds the strength of many soft

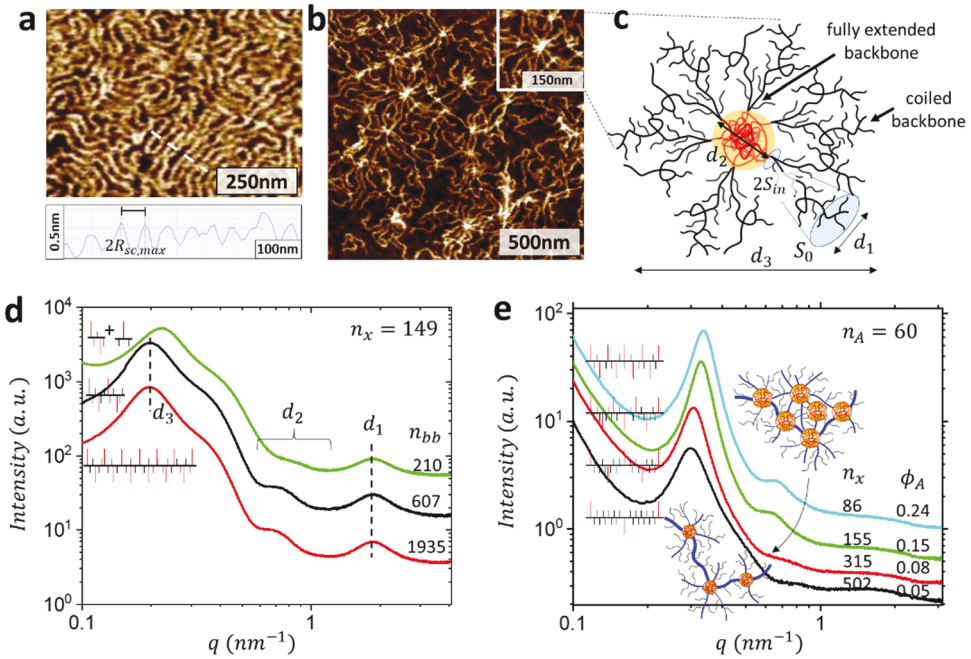

Fig. 3 Structural characterization of A-*g*-B brush copolymers by atomic force microscopy (AFM) and small angle X-ray scattering (SAXS). (a) AFM micrograph of a Langmuir–Blodget monolayer of PMMA-*g*-PDMS (n_g = 1, n_A = 81, n_x = 149) shows densely packed worm-like macromolecules separated by a distance $d \cong 2R_{sc,max}$, where $R_{sc,max}$ is a contour length of PDMS side chain. The cross-sectional profile was measured perpendicular to the molecular orientation (dashed line). (b) AFM micrograph of a sparse monolayer exhibits star-like aggregates due to association of A-blocks. (c) Dimensions of A-*g*-B network morphology: d_1 – interbrush distance, d_2 – A-domain diameter, d_3 – interdomain distance, S_{in} – interfacial area per brush strand at the domain surface, S_0 – bottlebrush packing area in the bulk. (d) SAXS curves of PMMA-*g*-PDMS (n_g = 1) samples with identical [n_{sc} = 14, $n_A \cong 60$, n_x = 149] yet different numbers of A-blocks per bottlebrush (z) as indicated. The n_{bb} variation does not cause any significant effects on the network morphology. The deviation of the green curve is due to $z = 1.4 < 2$, indicating that some molecules may have only one A block (loose ends) that lead to a smaller domain size (d_2) and correspondingly smaller distance between the domains (d_3) (Table 1). (e) SAXS curves of PS-*g*-PDMS (n_g = 8) samples with identical [n_{sc} = 14, n_g = 8, n_A = 60] yet different n_x and corresponding ϕ_A values. For this sample series, the bottlebrush peak is broader and shifts towards higher d_1 values because of possible interpenetration of side chains and backbone folding inside the bottlebrush envelope promoted by the decrease in grafting density.[40] The increase of ϕ_A at a given n_A results in the corresponding increase in the aggregation number, Q, and decrease of the interfacial area per brush strand, S_{in} (Table 1).

tissues such as aorta, blood vessel, skeletal muscle, and even some cartilage tissues (ESI,† Table S1).

Concurrent with the elastic response measured a low strain rate of $\dot{\varepsilon}$ = 0.005 s^{-1} (Fig. 4a and b), which corresponds to the rubber-elastic plateau for the PS-*g*-PDMS samples, the A-*g*-B architecture allows tuning the viscoelastic response. The frequency dependence of the storage modulus and damping factor was measured for samples varying (i) n_x at a given n_A (Fig. 4c), (ii) n_A at a given n_x, and (iii) grafting density, $\sim n_g^{-1}$ (ESI,† Fig. S26 and S27). The lowering of the crosslink density at a given n_A = 60 results in two effects (Fig. 4c): (i) decrease of the storage modulus (G'), which is consistent with the stress–elongation curves in Fig. 4b, and (ii) lower frequency shift of the elastic plateau onset, which is evidenced by the corresponding increase of the damping ($\tan\delta$). Other structural levers, such as grafting density, may be utilized as well to regulate viscoelastic behavior (ESI,† Fig. S26). However, nearly full replication of tissues viscoelastic response is achieved by leveraging both architecture and chemistry of A-*g*-B networks. While a PS-*g*-PDMS (n_g = 8) sample shows near identical damping response to ligament, replacing PDMS with a higher glass transition PIB in PS-*g*-PIB (n_g = 8) shifts the frequency spectrum demonstrating damping similar to porcine brain (Fig. 4d).

The effect of deformation on A-*g*-B network morphology was studied by *in situ* SAXS which allows instantaneous monitoring of changes in the d_1, d_2, and d_3 spacings during uniaxial extension (Fig. 5a). The strongest effect is observed for the inter-domain distance d_3, which progressively increases along the stretching axis while decreasing in the perpendicular directions as expected for uniaxial network deformation (Fig. 5b). In a similar fashion, the A-domain exhibits anisotropic variations: increasing along the stretching direction and decreasing in the perpendicular directions (Fig. 5c), which contrasts the lack of domain deformation in ABA elastomer.[13,15] The observed deformation of PMMA domains suggests a higher stress exerted on the nanospheres through two bottlebrush blocks attached to one A-block, which is consistent with the smaller bottlebrush footprint (S_{in}) (Table 1). However, the domains deformation does not lead to any detectable decrease of their average volume, which supports the hypothesis of re-association of dislodged A-blocks with neighboring domains in the course of the deformation process. Stretching also affects the brush diameter corresponding to the d_1 peak position (Fig. 5d), which is ascribed to unravelling of the backbone inside bottlebrush envelopes which contributes to strain-stiffening.[15]

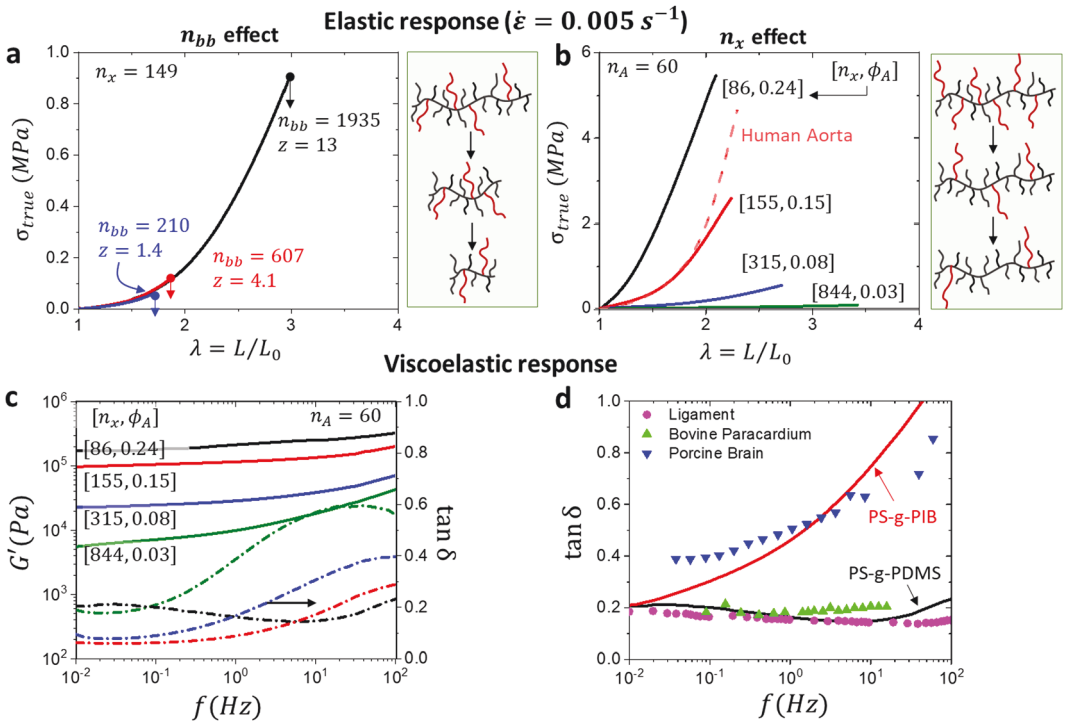

Fig. 4 (a) Strength of PMMA-*g*-PDMS (n_g = 1) elastomers systematically increases with the number of A blocks per A-*g*-B macromolecules, *z*, at a constant DP between A blocks of n_x = 149 (Table 1). (b) Stress–elongation curves of PS-*g*-PDMS (n_g = 8) samples with different n_x (and correspondingly ϕ_A) values as indicated (Table 1). The decrease of n_x at a given n_A = 60 results in progressively increasing strength. (c) Frequency sweeps of the storage modulus (*G*′) and damping factor (tan *δ*) of the PS-*g*-PDMS samples with different n_x and ϕ_A values from panel b. (d) PS-*g*-PDMS elastomer (n_g = 8, n_x = 86, n_A = 60) replicates the frequency dependence of the pericardium and ligament damping factors. Replacing of PDMS with PIB in the PS-*g*-PIB elastomer (n_g = 8, n_x = 216, n_A = 60) allows closely matching the damping of brain tissue (Table S1, ESI†).

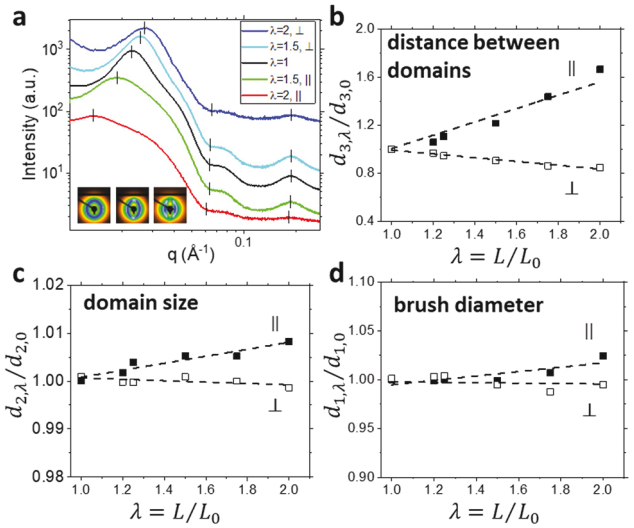

Fig. 5 *In situ* SAXS monitoring A-*g*-B elastomer deformation of PMMA-*g*-PDMS (n_g = 1, n_{bb} = 1935, ϕ_A = 0.044). (a) 1D SAXS curves and 2D patterns captured during uniaxial extension at different elongation ratios $\lambda = L/L_0$, as indicated. Normalized (b) inter-domain distance (c) domain diameter, and (d) brush diameter as a function of λ. Filled and hollow squares are measurements in the parallel and perpendicular planes, respectively.

Chemistry variation and application

In addition to controlling mechanical properties of thermoplastic elastomers, the modular nature of the A-*g*-B platform allows a broad range of chemical compositions for A and B blocks. The chemical variability accommodates specific functions such as thermal stability, adhesion, and molding (Fig. 1), while their mechanical properties (softness, firmness, and strength) are regulated by network architecture. To that end, we report exemplary A-*g*-B chemical structures that target specific application needs (Fig. 6a). First, using PDMS side chains and PMMA A-blocks in the above discussed PMMA-*g*-PDMS system (Fig. 6b) is beneficial for thermal stability of mechanical properties. The combination of a low glass transition temperature of PDMS (T_g = −124 °C) and highly cohesive PMMA domains maintains nearly constant storage and loss moduli within broad temperature (<100 °C) and frequency ranges (10^{-2}–10^2 Hz), which is valuable for devices subjected to considerable thermal fluctuations. However, other applications, *e.g.*, injection molding and 3D-printing, require fluidity at moderate temperatures. This was achieved by replacing PMMA with less cohesive PS as A-block, resulting in a storage modulus, *G*′, decrease above the PS glass transition temperature of 105 °C and demonstrating an elastomer-to-melt transition at 150 °C (Fig. 6b). The enhanced fluidity of the PS block enables injection molding and 3D printing of various shapes (Fig. 6c and ESI,† Section S2.5) that match the deformation response (modulus, strength, and elongation-at-break) of solution cast samples (ESI,† Fig. S31).

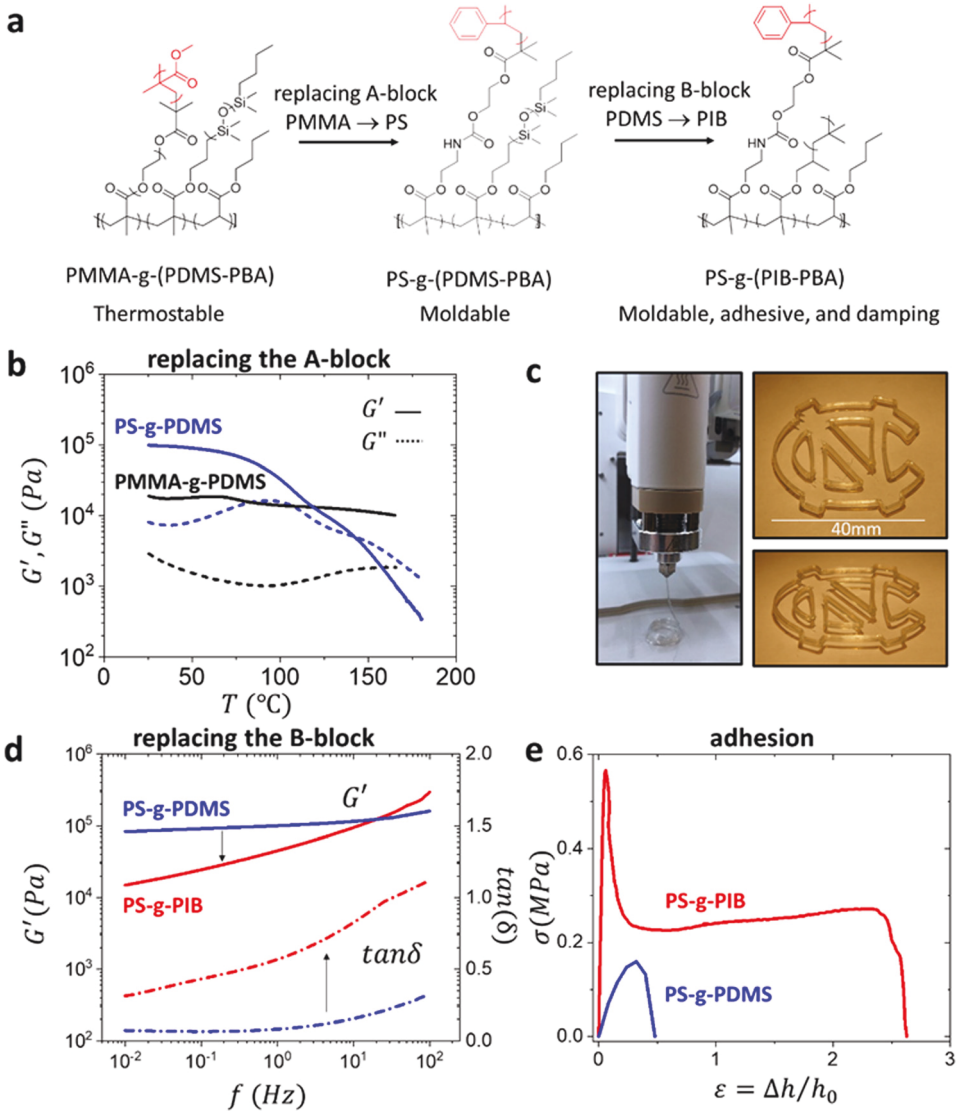

Fig. 6 (a) Copolymer structure of distinct A-*g*-B macromolecules utilized as mesoblocks for enhancing thermostability, moldability at lower temperatures, adhesion, and vibration damping. (b) Temperature dependence of storage (G') and loss (G'') moduli of A-*g*-B elastomers with chemically different A-blocks (PMMA and PS) yet the same bottlebrush B block with PDMS side chains (f = 1 Hz). Unlike the PS-*g*-PMMA sample, PS-*g*-PDMS (n_g = 8) elastomers undergoes melting at ~150 °C. (c) 3D printing of the UNC logo (photographs) was performed by fused filament fabrication using a PS-*g*-PIB (n_g = 8) sample at 150 °C. (d) Time-dependent and independent A-*g*-B brush copolymers in the PSA viscoelastic window. (e) Probe tack test of the PS-*g*-PIB and PS-*g*-PDMS samples (T = 25, $\dot{\varepsilon}$ = 1 s^{-1}, h_0 = 1 mm) reveals a considerable difference in the work of adhesion $W_{adh} = h_0\int_0^{\varepsilon_{max}} \sigma_{eng}(\varepsilon)d\varepsilon$ of 563 J m^{-2} and 50 J m^{-2}, respectively.

In other domains of practical applications, pressure sensitive adhesives and vibration damping, materials are expected to demonstrate a particular viscoelastic variance as a function of frequency (within the 10^{-2} to 10^{2} Hz range) at room temperature.[54] This feature can be addressed by substitution of PDMS with polyisobutylene (PIB) side chains (Fig. 6a), which shifts the material relaxation dynamics toward the Rouse regime at room temperature (Fig. 6d). The combination of lowering the storage modulus ($G' < 0.1$ MPa at 0.01 Hz) and enhanced viscoelasticity (increase of $\tan\delta = G''/G'$ from ~0.1 to ~1 range) facilitates substrate wetting and energy dissipation at a debonding rate of ~1 Hz. This results in the increase of the overall work of adhesion (W_{adh}) of the material by probe tack testing showing potential as a pressure sensitive adhesive (Fig. 6e and ESI,† Section S2.6). The chemistries addressed are merely a subset of synthetic and application pathways capable of implementing A-*g*-B brush architecture and can be greatly expanded.

Conclusions

The A-*g*-B brush platform enables immense expansion of the mechanical property scope of thermoplastic elastomers by independently tuning elastic and viscoelastic properties. Specifically, a unique combination of softness, firmness, and strength was attained through coordinated variation of the side chain length,

grafting density, volume fraction of A blocks, and interconnectivity network cells. Furthermore, specific properties like molding, damping, and pressure sensitive adhesion were adjusted by varying the chemical composition of the A and B blocks. Specifically, A-*g*-B materials achieved strength of ~10 MPa, exceeding that of blood vessels, and closely replicated frequency dependence of the damping factor of super-soft brain and super-tough ligament tissues. The thermoplastic nature of A-*g*-B networks combined with reduced viscosity of brush-like macromolecules enables injection molding and 3D printing of shapes with molecularly tunable tissue-mimetic elastic and dynamic mechanical properties.

Author contributions

E. D., M. M., and A. N. K. equally contributed to this study, synthesized and characterized A-*g*-B brush copolymers; F. V., M. M., and E. D. performed fused filament fabrication 3D printing; V. K. conducted reactivity studies; Y. D. G. performed computer simulations, E. Y. K. conceived the idea of injection molding; E. A. B., E. A. N., and D. A. I. performed SAXS experiments and analysis; Y. T., and A. V. D. provided theoretical analysis of mechanical properties and computer simulations of self-assembled network deformations; M. V. V. and S. S. conceived the idea of the A-*g*-B platform; M. M. and S. S. S. were primary writers of the manuscript. All authors discussed the results and provided feedback on the manuscript.

Conflicts of interest

There are no conflicts to declare.

Acknowledgements

The authors gratefully acknowledge funding from the National Science Foundation (DMR 1921835, 1921858, 1921923, DMR 2049518, and DMR 2004048). Y. D. G. and E. Y. K. acknowledge funding from the Russian Science Foundation (RSF grant 19-13-00340-II). The authors acknowledge technical support from the personnel of the ID02 and BM26 beamlines of the ESRF in Grenoble (France).

References

1 L. G. Griffith and G. Naughton, *Science*, 2002, **295**, 1009–1014.
2 S. Lv, D. M. Dudek, Y. Cao, M. M. Balamurali, J. Gosline and H. Li, *Nature*, 2010, **465**, 69–73.
3 M. A. Meyers, P.-Y. Chen, A. Y.-M. Lin and Y. Seki, *Prog. Mater. Sci.*, 2008, **53**, 1–206.
4 F. H. Silver, J. W. Freeman and D. DeVore, *Skin Res. Technol.*, 2001, **7**, 18–23.
5 B. Rashid, M. Destrade and M. D. Gilchrist, *J. Mech. Behav. Biomed. Mater.*, 2014, **33**, 43–54.
6 G. A. Holzapfel, G. Sommer, C. T. Gasser and P. Regitnig, *Am. J. Physiol. Heart Circ. Physiol.*, 2005, **289**, H2048–H2058.
7 B. Zhou, F. Xu, C. Q. Chen and T. J. Lu, *Philos. Trans. R. Soc., A*, 2010, **368**, 679–690.
8 L. D. Muiznieks and F. W. Keeley, *Biochim. Biophys. Acta, Mol. Basis Dis.*, 2013, **1832**, 866–875.
9 F. H. Silver, P. B. Snowhill and D. J. Foran, *Ann. Biomed. Eng.*, 2003, **31**, 793–803.
10 C. D. Kuthe and R. V. Uddanwadiker, *J. Appl. Biomater. Funct. Mater.*, 2016, **14**, 154–162.
11 D. Zhalmuratova, T.-G. La, K. T.-T. Yu, A. R. A. Szojka, S. H. J. Andrews, A. B. Adesida, C. Kim, D. S. Nobes, D. H. Freed and H.-J. Chung, *ACS Appl. Mater. Interfaces*, 2019, **11**, 33323–33335.
12 B. Depalle, Z. Qin, S. J. Shefelbine and M. J. Buehler, *J. Mech. Behav. Biomed. Mater.*, 2015, **52**, 1–13.
13 M. Vatankhah-Varnosfaderani, A. N. Keith, Y. Cong, H. Liang, M. Rosenthal, M. Sztucki, C. Clair, S. Magonov, D. A. Ivanov, A. V. Dobrynin and S. S. Sheiko, *Science*, 2018, **359**, 1509–1513.
14 M. Vatankhah-Varnosfaderani, W. F. M. Daniel, M. H. Everhart, A. A. Pandya, H. Liang, K. Matyjaszewski, A. V. Dobrynin and S. S. Sheiko, *Nature*, 2017, **549**, 497–501.
15 A. N. Keith, M. Vatankhah-Varnosfaderani, C. Clair, F. Fahimipour, E. Dashtimoghadam, A. Lallam, M. Sztucki, D. A. Ivanov, H. Liang, A. V. Dobrynin and S. S. Sheiko, *ACS Cent. Sci.*, 2020, **6**, 413–419.
16 T. T. Duncan, E. P. Chan and K. L. Beers, *ACS Appl. Mater. Interfaces*, 2019, **11**, 45310–45318.
17 J.-H. So, A. S. Tayi, F. Güder and G. M. Whitesides, *Adv. Funct. Mater.*, 2014, **24**, 7197–7204.
18 C. Storm, J. J. Pastore, F. C. MacKintosh, T. C. Lubensky and P. A. Janmey, *Nature*, 2005, **435**, 191–194.
19 J. P. Gong, *Science*, 2014, **344**, 161–162.
20 E. Ducrot, Y. Chen, M. Bulters, R. P. Sijbesma and C. Creton, *Science*, 2014, **344**, 186–189.
21 J. p Gong, Y. Katsuyama, T. Kurokawa and Y. Osada, *Adv. Mater.*, 2003, **15**, 1155–1158.
22 J. Zhang, A. N. Keith, S. S. Sheiko, X. Wang and Z. Wang, *ACS Appl. Mater. Interfaces*, 2021, **13**, 3278–3286.
23 Y. You, J. Yang, Q. Zheng, N. Wu, Z. Lv and Z. Jiang, *Sci. Rep.*, 2020, **10**, 11727.
24 V. R. Feig, H. Tran, M. Lee and Z. Bao, *Nat. Commun.*, 2018, **9**, 2740.
25 T. Pakula, Y. Zhang, K. Matyjaszewski, H. Lee, H. Boerner, S. Qin and G. C. Berry, *Polymer*, 2006, **47**, 7198–7206.
26 L. J. Fetters, D. J. Lohse, C. A. García-Franco, P. Brant and D. Richter, *Macromolecules*, 2002, **35**, 10096–10101.
27 D. Vlassopoulos, G. Fytas, B. Loppinet, F. Isel, P. Lutz and H. Benoit, *Macromolecules*, 2000, **33**, 5960–5969.
28 M. Hu, Y. Xia, G. B. McKenna, J. A. Kornfield and R. H. Grubbs, *Macromolecules*, 2011, **44**, 6935–6943.
29 M. Abbasi, L. Faust, K. Riazi and M. Wilhelm, *Macromolecules*, 2017, **50**, 5964–5977.
30 I. N. Haugan, M. J. Maher, A. B. Chang, T.-P. Lin, R. H. Grubbs, M. A. Hillmyer and F. S. Bates, *ACS Macro Lett.*, 2018, **7**, 525–530.
31 H. Liang, B. J. Morgan, G. Xie, M. R. Martinez, E. B. Zhulina, K. Matyjaszewski, S. S. Sheiko and A. V. Dobrynin, *Macromolecules*, 2018, **51**, 10028–10039.

32 W. F. M. Daniel, J. Burdyńska, M. Vatankhah-Varnoosfaderani, K. Matyjaszewski, J. Paturej, M. Rubinstein, A. V. Dobrynin and S. S. Sheiko, *Nat. Mater.*, 2016, **15**, 183–189.
33 R. Xie, S. Mukherjee, A. E. Levi, V. G. Reynolds, H. Wang, M. L. Chabinyc and C. M. Bates, *Sci. Adv.*, 2020, **6**, eabc6900.
34 A. V. Dobrynin and J.-M. Y. Carrillo, *Macromolecules*, 2011, **44**, 140–146.
35 M. Maw, B. J. Morgan, E. Dashtimoghadam, Y. Tian, E. A. Bersenev, A. V. Maryasevskaya, D. A. Ivanov, K. Matyjaszewski, A. V. Dobrynin and S. S. Sheiko, *Macromolecules*, 2022, **55**, 2940–2951.
36 H. Liang, Z. Wang and A. V. Dobrynin, *Macromolecules*, 2019, **52**, 8617–8624.
37 L. Yu, E. R. Newton, D. C. Gillis, K. Sun, B. C. Cooley, A. N. Keith, S. S. Sheiko, N. D. Tsihlis and M. R. Kibbe, *Biomater. Sci.*, 2021, **9**, 5160–5174.
38 Z.-H. Guo, A. N. Le, X. Feng, Y. Choo, B. Liu, D. Wang, Z. Wan, Y. Gu, J. Zhao, V. Li, C. O. Osuji, J. A. Johnson and M. Zhong, *Angew. Chem., Int. Ed.*, 2018, **57**, 8493–8497.
39 J. Pyun, T. Kowalewski and K. Matyjaszewski, *Macromol. Rapid Commun.*, 2003, **24**, 1043–1059.
40 K. Matyjaszewski, *Adv. Mater.*, 2018, **30**, 1706441.
41 N. P. Truong, G. R. Jones, K. G. E. Bradford, D. Konkolewicz and A. Anastasaki, *Nat. Rev. Chem.*, 2021, **5**, 859–869.
42 S. Perrier, *Macromolecules*, 2017, **50**, 7433–7447.
43 J. Chiefari, Y. K. (Bill) Chong, F. Ercole, J. Krstina, J. Jeffery, T. P. T. Le, R. T. A. Mayadunne, G. F. Meijs, C. L. Moad, G. Moad, E. Rizzardo and S. H. Thang, *Macromolecules*, 1998, **31**, 5559–5562.
44 S. C. Radzinski, J. C. Foster, R. C. Chapleski Jr, D. Troya and J. B. Matson, *J. Am. Chem. Soc.*, 2016, **138**, 6998–7004.
45 D. Uhrig and J. W. Mays, *Macromolecules*, 2002, **35**, 7182–7190.
46 J. Bolton and J. Rzayev, *Macromolecules*, 2014, **47**, 2864–2874.
47 A. L. Liberman-Martin, C. K. Chu and R. H. Grubbs, *Macromol. Rapid Commun.*, 2017, **38**, 1700058.
48 D.-P. Song, T. H. Zhao, G. Guidetti, S. Vignolini and R. M. Parker, *ACS Nano*, 2019, **13**, 1764–1771.
49 E. B. Zhulina, S. S. Sheiko, A. V. Dobrynin and O. V. Borisov, *Macromolecules*, 2020, **53**, 2582–2593.
50 J. M. Sarapas, T. B. Martin, A. Chremos, J. F. Douglas and K. L. Beers, *Proc. Natl. Acad. Sci. U. S. A.*, 2020, **117**, 5168–5175.
51 C. R. López-Barrón, J. R. Hagadorn, S. J. Mattler and J. A. Throckmorton, *Macromolecules*, 2020, **53**, 3778–3788.
52 A. N. Keith, C. Clair, A. Lallam, E. A. Bersenev, D. A. Ivanov, Y. Tian, A. V. Dobrynin and S. S. Sheiko, *Macromolecules*, 2020, **53**, 9306–9312.
53 C. Clair, A. Lallam, M. Rosenthal, M. Sztucki, M. Vatankhah-Varnosfaderani, A. N. Keith, Y. Cong, H. Liang, A. V. Dobrynin, S. S. Sheiko and D. A. Ivanov, *ACS Macro Lett.*, 2019, **8**, 530–534.
54 E. P. Chang, *J. Adhes.*, 1991, **34**, 189–200.